

Analysis of microchannel plate response in relation to pulsed laser time-of-flight photoemission spectroscopy

D. C. Anacker and J. L. Erskine
Department of Physics, University of Texas, Austin, Texas 78712

(Received 19 November 1990; accepted for publication 14 January 1991)

Design considerations, construction details, performance evaluation, and experimental tests of a time-of-flight photoelectron spectrometer utilizing a pulsed laser source are presented. The new spectrometer has been designed for heat transport and carrier dynamics studies of solid surfaces using femtosecond laser excitation. Special attention is directed to analysis of the dynamic range and linearity of the detector in order to obtain quantitative information from measured electron yields.

I. INTRODUCTION

The combination of ultra-short-pulse laser technology with photoelectron emission detection offers important new opportunities for probing the properties of matter. Recent examples include studies of electron heat transport and cooling dynamics on a femtosecond time scale,¹⁻³ studies of interband and intraband lifetimes of image potential states by two-photon photoemission techniques,⁴⁻⁶ and measurements of transient high-temperature electron distributions in laser generated solid density plasmas.⁷⁻⁹ Time-of-flight techniques provide an optimum method for analyzing the energy distribution of low energy electrons ($KE < 20$ eV) produced by laser excitation in many cases of practical interest.¹⁰

This article describes design considerations, construction details, and performance tests of a time-of-flight photoelectron spectrometer that utilizes a femtosecond laser source. Various factors affecting the energy resolution, dynamic range, linear response, and overall efficiency are discussed. Construction details required to achieve optimum performance are presented along with results of diagnostic tests of the anode using time domain reflectometry. Performance evaluation tests and results of initial experiments utilizing the spectrometer are also presented.

II. GENERAL CONSIDERATIONS

The analyzer described here is specifically intended to measure the angle and energy distribution of electrons produced by pulsed laser excitation of solids. The kinetic energy range of electrons produced by direct quantum excitations is limited by the laser wavelength. Nonlinear effects in the excitation can produce multiphoton excitations; in addition, laser energies can also be doubled, tripled, etc., to energies in the vacuum ultraviolet (above 12 eV). More important, focused beams from short pulse high power lasers can produce heating sufficient to generate hot plasmas having electron temperatures of several million degrees. Corresponding electron energies are several hundred eV. At the higher energies (> 20 eV), extremely high energy resolution is not required, but for measurements dealing with quantum excitations (< 20 eV typically) good energy resolution is desirable. Very short pulses (100 femtoseconds) can be monochromatic to a resolution of about 100 meV (limited by the uncer-

tainty relation $\Delta E \Delta t \geq \hbar/2$); however, intrinsic broadening of photoemission peaks resulting from excitations more than a few hundred meV from the Fermi energy E_F is generally 100 meV or more. Thermal effects at room temperature also yield intrinsic line widths of ~ 100 meV; therefore, an energy resolution of 50–100 meV in the kinetic energy range below 10 eV should satisfy all reasonable requirements. Angular resolution of a few degrees is quite adequate for probing wavevector dependencies because Δk_{\parallel} for $\pm 1^\circ$ angular resolution and electron energy < 5 eV is small compared with a Brillouin zone dimension.

A time-of-flight instrument seems to offer an ideal solution for filling the above requirements, although there remain a few other factors that must be considered—primarily, the electron flux and its temporal characteristics. Since these factors mainly affect the dynamic range of the spectrometer and are primarily associated with the response of the gain medium (in this case, a pair of microchannel plates), they are discussed later.

In a time-of-flight energy analyzer (shown schematically in Fig. 1), electrons are created and interact during a brief time interval, subsequently moving at near constant velocity in a field free region to a suitable detector located a distance L_d from the source region. In the sense that measurement of characteristics of free asymptotic scattering distributions is generally required to link scattering theory and experiments, it is inherently desirable to select a drift tube length L_d large compared to the interaction region.

Several errors resulting from measuring velocity by the drift tube method are also minimized by lengthening the drift tube. A relation facilitating discussion of error is

$$V_n = \frac{L_d}{t_n} + \frac{1}{mt_n} \int_0^{t_n} te^{-E[x(t),t]} dt, \quad (1)$$

obtainable from integration by parts of

$$L_d = \int_0^{t_n} V dt.$$

By means of this equation, basically, the distribution of source-to-detector flight times t_n represents the distribution of asymptotic velocities V_n (or energies) of electrons produced in the source region. The electric field includes contributions from space charge, sample image charge, induced chamber wall charges, rendering specific evaluation of the

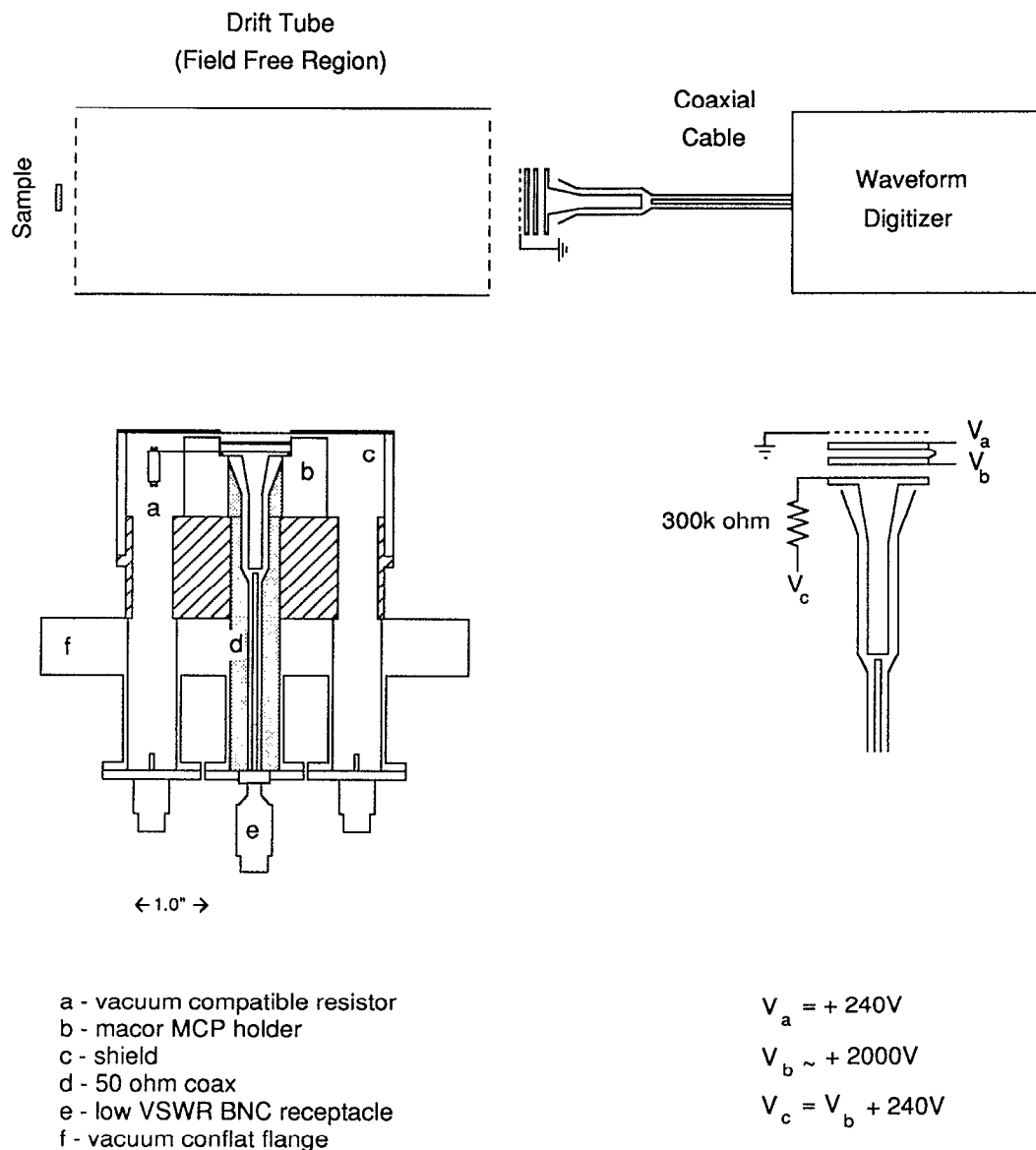


FIG. 1. Time-of-flight energy analyzer schematic, electron detector construction, and biasing detail.

integral difficult. Nevertheless, one expects that in most cases, the interaction region extends essentially a limited distance into the drift tube, if at all, making the integral L_d independent and the second term proportional to L_d^{-1} (since $1/mt_n \sim V_n/(mL_d)$). If, as is conventional, only the remaining expression is utilized, $V_n = L_d/t_n$, one is still confronted with sources of error, including finite electron multiplier response time. This error also diminishes as L_d^{-1} ($dV_n = -V_n L_d^{-1} dt$); these several motivations for adopting a very long drift tube must be balanced against physical inconvenience and magnetic shielding requirements which both increase with drift tube length. The previously introduced concept of a minimum acceptable energy resolution for the instrument (100 meV for our intended application) affords one logical way to select a compromise length.

Energy resolution of a time-of-flight detector depends on geometrical factors (finite source size and variations in

source-to-detector distance caused by a nonspherical detector) and on the detector response. Corresponding geometrical effects occur and have been analysed in dispersive-type analysers and simple retarding grid analysers.^{11,12} In the present case, the source size defined by the laser beam is negligible compared to the drift tube length $L_d = 0.4$ m, and the detector area $A = 2.48$ cm² subtends an angle of approximately 1°. Under these conditions, geometrical effects contribute negligibly to the reduction of energy resolution that depends primarily on the detection system response function.

Figure 2 illustrates the relationship between electron flight time t , electron kinetic energy E , and drift tube length L . The first derivative of flight time with energy dt/dE expresses the time resolution (as a function of E and L) required to achieve a given energy resolution. Channeltron detectors deliver typical electron gains of $G \sim 10^8$, pulse rise

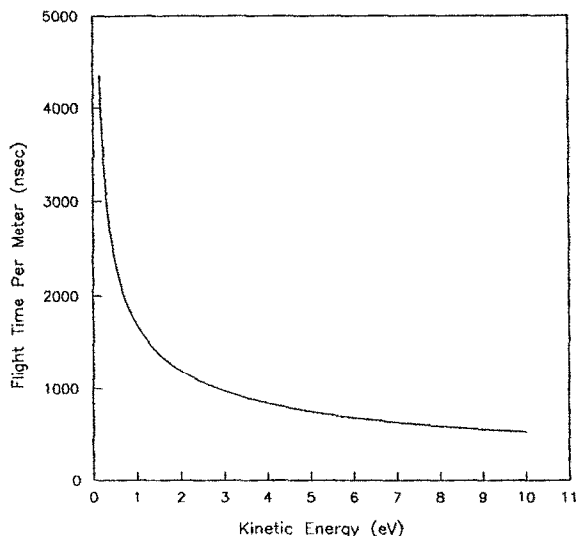


FIG. 2. Plot of electron flight time t per meter length of drift tube vs electron kinetic energy. dt/dE represents the relationship between time resolution required to achieve a given energy resolution at E .

times of 3–5 ns and pulse widths of 18–20 ns. Microchannel plates (MCPs) yield typical electron gains of $G \sim 10^6$ – 10^7 (chevron pair) and pulse widths of 300 ps (single microchannel plate) or 1 ns (chevron pair). Electron gains of $\sim 10^7$ are required for direct coupling into a fast scope or waveform digitizer, therefore, an overall detector response time of the order of a few ns represents a good basis for selection of other system components. Transient waveform digitizers are available with step response risetimes less than 2 ns that can record single shot waveforms with time resolution comparable to the channelplate response.

Figure 3 presents a plot of time-of-flight energy resolution (per meter of drift tube length) as a function of electron energy for three values of instrument response function. Based on the fact that a 2 ns full width half maximum (FWHM) response to a δ function can be achieved, the energy resolution at 10 eV kinetic energy for a $\frac{1}{2}$ m drift tube is ~ 150 meV which is adequate for our intended application.

III. CONSTRUCTION DETAILS AND QUALIFICATION TESTS

Figure 1 illustrates construction details of our electron detection system. A 4-in.-diam $\frac{1}{2}$ -m-long drift tube permits resolution represented by curve C of Fig. 3. The sample region and drift tube are shielded by a single μ -metal tube that yields a residual field of 4 milligauss.

Our chevron pair consists of 1-in.-diam resistively matched Varian VUW-8960 channelplates spaced 0.01 in. apart. A coaxial conductor, drawn to scale in the detailed cutaway view of Fig. 1, transmits the amplified signal from a 1-in.-diam anode to a conventional 50 Ω BNC vacuum feedthrough. The inner and outer radii of this conductor are tapered with a consistent 2.37:1 ratio in order to obtain impedance matching to the 50 Ω cable. Decoupling of high anode voltage from the waveform analyser is accomplished by means of a small gap (0.06 in.) in the coaxial conductor.

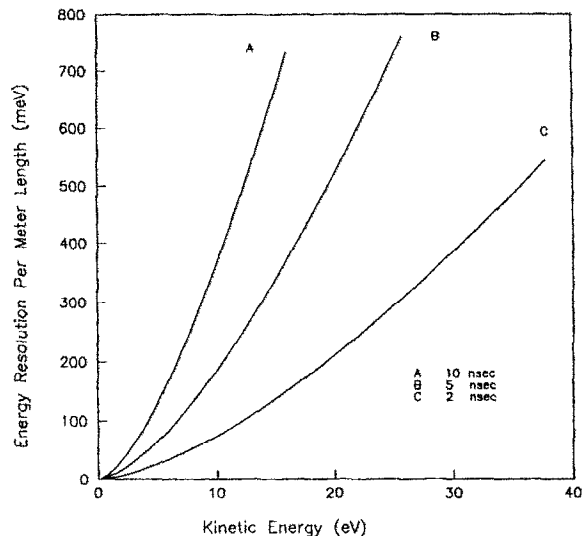


FIG. 3. Plot of spectrometer energy resolution (per meter drift tube length) vs electron kinetic energy for three values of instrument response time (FWHM of δ -function response).

To minimize distortion of high frequency signal components a low VSWR rated feedthrough (Ceramaseal 807B0549-02-W) is used to provide signal connection. Typical electrical biasing is shown in Fig. 1. Signal propagation and multiple reflection associated with the anode biasing line is reduced by placing a large (vacuum compatible) series resistance immediately adjacent to the anode, as shown. Time domain reflectometer (TDR) tests illustrated in Fig. 4 indicate that the electrical response of the completed feedthrough-tapered coax-anode combination essentially matches that of an open ended length of 50 Ω standard RG58 C/U cable. We measure a rise time of 245 ps for reflection of a TDR pulse at a cable open end and 350 ps when connected to the detector. This TDR data corresponding to the above described design indicates no significant distortion from potential reflection points such as the signal vacuum feedthrough, coaxial conductor gap, and anode biasing circuit.

IV. TESTS AND PERFORMANCE

To verify the implications of our TDR studies (that the post chevron signal path effectively matches the 50 Ω transmission line and hence should induce no distortion) we were able to measure the detection system response to a δ -function like excitation. An amplified CPM dye laser providing 10 Hz, 620 nm, 0.05 Joule, 100 fs FWHM light pulses was directed so that near specularly reflected light from a polished silver target illuminated the front MCP. The signal recorded with a waveform digitizer (Tektronix 7912AD) triggered off the 10 Hz laser amplifier is shown in Fig. 5. Given the essential δ -function character of the input current at the anode, conventional mathematical arguments immediately imply that Fig. 5 is the response function of the post chevron portion of the detection system. TOF data, so far obtained or anticipated, would not significantly change under deconvolution with such a narrow—2 ns FWHM—response function.

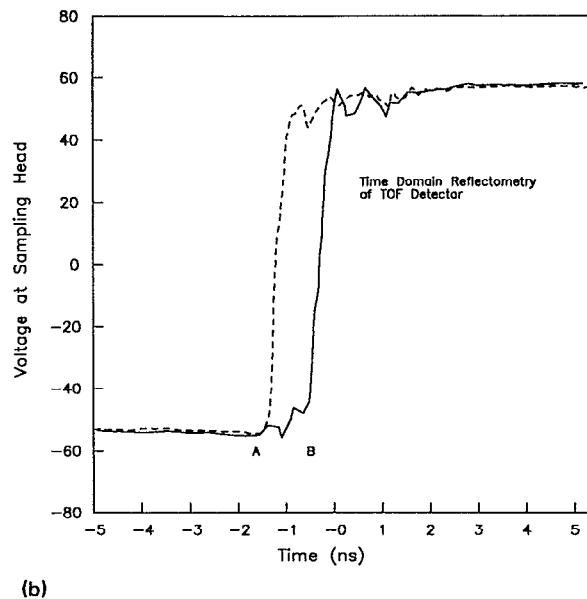
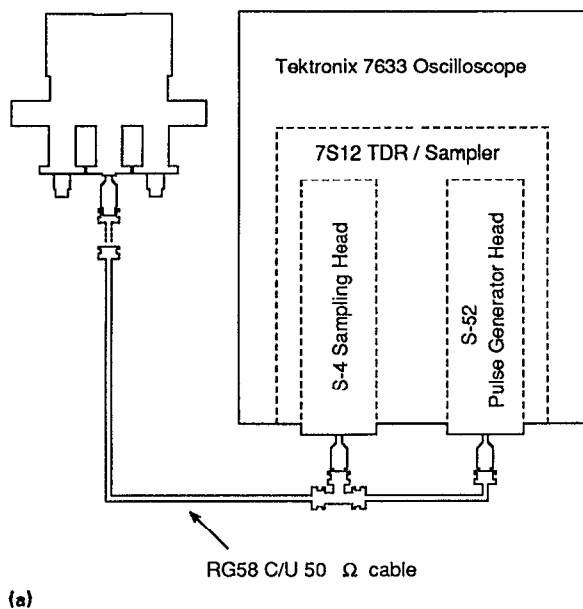


FIG. 4. (a) Schematic diagram of time delay reflectometry tests of detector transmission characteristics. (b) Comparative responses to 25 ps rise time TDR pulse of open-ended 50 Ω coaxial cable (dashed) and cable connected to TOF detector (solid). A and B mark the time delay positions of the 50 Ω cable end and the TOF anode, respectively.

V. MICROCHANNEL PLATE RESPONSE

Since the total response function of the detection system is a convolution of the MCP response function with the response of other detection system components, it is important to determine what criteria must be met by an electron pulse to be profiled so that it is not distorted by gain nonlinearities in either the front or rear MCP. For the front MCP, a well-known criteria for linear response is that the expected interval between successive electrons entering the same individual pore exceed the single channel dead time τ . It is quite commonly possible to estimate or measure the net sample

photoemission rate—sometimes an electrometer attached to the sample ground wire has sufficient sensitivity. Necessary and sufficient conditions for the above criterion to be met are given by the two formulas

$$(\text{OAR})(\#e^-/\text{pulse})\alpha_F < N_c, \quad (2)$$

$$\frac{(\text{OAR})\alpha_F(\text{rep rate})(\#e^-/\text{pulse})}{N_c} < \frac{1}{\tau}, \quad (3)$$

where α_F denotes the fraction of electron solid angle subtended by the exposed, active MCP area, N_c the number of exposed channels, and OAR the open area ratio of the MCP. The duality of conditions reflects the fact that the characteristic interval between single pore excitations can fall below τ for a repetitive laser excitation of the electron source if either the intensity per pulse or repetition rate are made sufficiently high.

No consensus has developed yet as to the single channel MCP recovery time; formulas predicated on single channel strip current,¹³ lumped capacitance,^{14,15} or distributed capacitance^{16,17} yield different values for τ of the order of a millisecond, generally. An infinite series solution to the pore recovery time problem has been described by Gatti and co-workers¹⁶; however, only in the artificial model of infinite uniform dielectric with isotropic conductivity is a relaxation rate extractable non-numerically. Fortunately, at least in the plate bias voltage regime where gain is limited by the decelerative effect of wall charge (sometimes ambiguously referred to as space charge), a simple recovery rate formula can be obtained for a realistic MCP model. Because our data was obtained in this operating voltage regime, it is useful to summarize the derivation. Figure 6 illustrates the relevant geometry. The discussion is confined to the period following multiplication during which any currents related to secondary emission have ceased. As is warranted by standard MCP

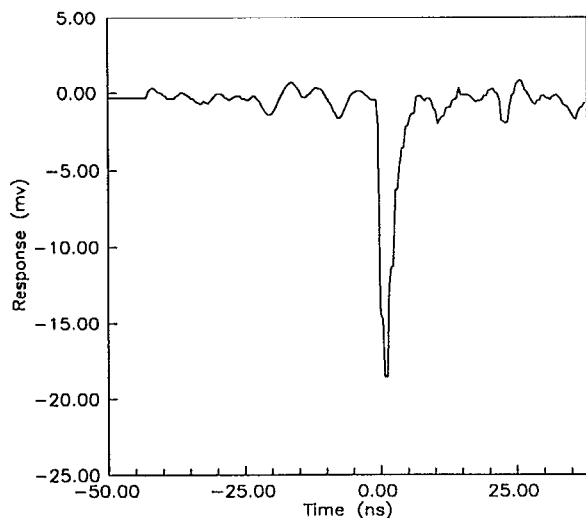


FIG. 5. Response of anode, tapered coax, digitizer system to 1 ns (δ function) excitation produced by 100 fs laser illumination of chevron. 2 ns FWHM provides an estimate of single electron time-of-flight (and hence energy) resolution.

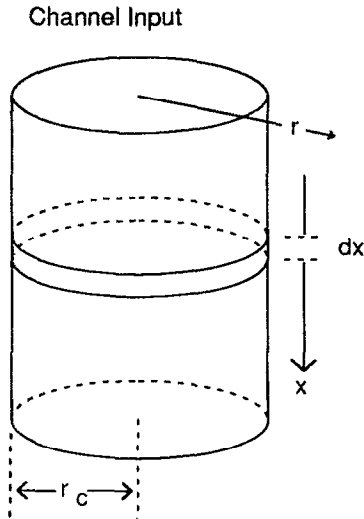


FIG. 6. Geometry relevant to derivation of single channel recovery time.

parameters, we assume that currents are confined to the agglomerated semiconducting lead surface of the channel¹⁴ and therefore introduce surface charge σ , surface current density J , and surface resistance R ($\text{s cm}^{-1}/\text{cm}^2$). Azimuthal symmetry about the channel axis reduces the non-zero field and current components to E_x , E_r , and J_x . For current flow through an annular surface element of width dx , Ohm's law yields

$$\begin{aligned} dV &= \langle E_x(x) \rangle dx \\ &= [R dx 2\pi r_c] [J_x(x+dx) - J_x(x)] 2\pi r_c, \end{aligned}$$

where

$$\langle E_x(x) \rangle = \frac{E_x(x+dx) + E_x(x)}{2},$$

and consequently

$$\frac{dE_x}{dx} = R 8\pi^2 r_c^2 \frac{dJ_x}{dx}. \quad (4)$$

For this geometry, the equation of continuity reduces to

$$\frac{dJ_x}{dx} + \frac{\partial \sigma}{\partial t} = 0, \quad (5)$$

and hence

$$\tau = \frac{\text{OAR}}{1 - \text{OAR}} \frac{1}{\pi} R_{\text{MCP}} \frac{\epsilon \{ [(1 - \text{OAR})/\text{OAR}] \pi r_c^2 (\# \text{channels per plate}) \}}{\text{MCP thickness}},$$

where R_{MCP} denotes the measured face-to-face resistance. Since the bracketed factor is the nonopen single plate area, and $\epsilon \gg \epsilon_0$ ($\epsilon \approx 8$), this formula is approximated well by

$$\tau = \frac{\text{OAR}}{1 - \text{OAR}} \frac{1}{\pi} R_{\text{MCP}} C_{\text{MCP}}, \quad (9)$$

where C_{MCP} is the measured face-to-face MCP capacitance. Typically, the OAR is about 0.5 and so this time constant is

$$\frac{dE_x}{dx}(r_c) = -8\pi^2 R r_c^2 \frac{\partial \sigma}{\partial t}$$

is valid. The tangential component of \mathbf{E} is always continuous, and so $E_x(r_c) = E_x(r_c^+)$, yielding the useable relation

$$\frac{dE_x}{dx}(r_c^+) = \frac{dE_x}{dx}(r_c).$$

Assuming $\tilde{\epsilon} = \epsilon$ times the identity matrix for $r_c < r < (D_{cc} - r_c)$, where D_{cc} is the center to center channel spacing, $\nabla \cdot \tilde{\epsilon} \mathbf{E} = 4\pi \rho$ implies (since the free charge density is confined to $r = r_c$)

$$\frac{dE_x}{dx} = \frac{dE_r}{dr}, \quad r_c < r < (D_{cc} - r_c),$$

and hence

$$\frac{dE_r}{dr}(r_c^+) = -8\pi^2 R r_c^2 \frac{\partial \sigma}{\partial t}. \quad (6)$$

$\tilde{\epsilon}$ approximates the actual dielectric response in the region $r_c < r < (D_{cc} - r_c)$ rather than denoting the response of a continuous dielectric modeling average properties of the MCP (as in Fig. 4.10 and corresponding formulae and Ref. 16). In order to compute E_r and thence dE_r/dr handily "Gaussian pillbox" techniques can be used, at saturation region points $x = x_s$ where the electron cascade self regulates itself¹⁴ to average unity gain at each bounce. The residual wall charge density is uniform in this region so that, ignoring end effects, it produces a radial field component given by

$$E_r(x_s, r) = \frac{r_c}{r} \sigma(x_s) \frac{4\pi}{\epsilon}, \quad r > r_c.$$

The surface charge in the channel after cessation of all secondary emission thereby relaxes with rate given by

$$\frac{\partial \sigma(x_s)}{\partial t} = \frac{-\sigma(x_s)}{r_c^3 \epsilon 2\pi R}. \quad (7)$$

Hence, in the saturation region at least, where most gain loss occurs,

$$\sigma(t) = \sigma(0) e^{-t/\tau},$$

where

$$\tau = r_c^3 \epsilon 2\pi R. \quad (8)$$

This value of τ can be recast as

generally about π^{-1} less than the result obtained by Gatti and co-workers¹⁶ ($\tau = R_{\text{MCP}} C_{\text{MCP}}$) for an infinite uniform dielectric of isotropic conductivity. It is interesting to consider then that time constants as high as $\approx 5 R_{\text{MCP}} C_{\text{MCP}}$ have been reported,¹⁷ some fifteen times our computed value of τ . A commonly cited experimental estimation of τ involves measuring the input flux at which MCP gain begins to deteriorate.^{14,17} The measurement must be conducted at a vol-

tage in the hard wall charge saturation regime (channel bias $\geq 8.94 (L/D) + 450 \text{ V}^{18}$) in order for measurably significant gain deterioration to occur when single channel excitation frequency begins to exceed the above saturation recovery rate. A relevant factor also derived from the study of Gatti and co-workers¹⁶ is that wall charging results in considerable electric field leakage into first and second neighbor channels. For a standard MCP example (with indicated G of 6.25×10^5), their numerical relaxation data shows that a radial field in excess of 4 V per channel spacing persists throughout $t - t_{\text{excitation}} < 3R_{\text{MCP}} C_{\text{MCP}}$ out to the second channel neighboring an excited pore. As will be elaborated on in a subsequent section, a lateral field of this magnitude perturbing the last 20% (or even more) of a channel where most gain occurs, is bound to severely attenuate gain in that channel. For any such MCP, the relaxation time measurement technique just described will obtain an erroneously high value by a factor equalling the total number of quiescent neighboring channels that a fired channel can deactivate by virtue of its perturbing field. Assuming validity of the temporarily deferred arguments for quiescent channel deadening, the MCP modeled in Ref. 16 is assumed to be operating at the upper end of normal single plate gain (6.25×10^5), and the eighteen first and second neighbor channels deactivated in this case indicate an upper bound for experimentally measured τ of 19 times our proposed theoretical single channel recovery time. If our theoretical τ formula is correct, one is thus led to predict a maximum experimentally measured τ of $19/\pi R_{\text{MCP}} C_{\text{MCP}}$, assuming OAR of 0.5, in good agreement with high experimental values reported.

Our front MCP has a gain of 10^4 or less at bias voltages providing acceptable gain linearity. Since lateral field strength scales roughly as wall charge per channel length and thereby approximately as the gain, one would predict a measurable dead time for our plates involving no neighbor channel gain deactivation factor. It therefore appears valid to assume

$$\tau = \frac{\text{OAR}}{1 - \text{OAR}} \frac{1}{\pi} R_{\text{MCP}} C_{\text{MCP}}$$

in our above cited conditions for front MCP linearity, provided front MCP gain is 10^4 or less.

Conditions insuring statistically equal multiplication in the rear MCP for each electron incident on a chevron pair during a short pulse are more difficult to ascertain. A first principal calculation of chevron linear response, let alone nonlinear behavior, has been characterized as a prohibitively complex many body calculation.¹⁸ The desirability of criteria and the inadequacy of the 10% strip current charge supply limit is indicated by data of Fig. 7. Curves A, B, and C are each multishot average TOF spectra from the same repetitive photoexcitation, but acquired with differing MCP bias levels, as indicated. Curves A and B are the same within a nearly constant proportionality factor—indicating linear gain response. Curve C at the highest plate voltage exhibits gain saturation for the electron tail. According to electrometer sample-to-ground current data, the flux incident on the front MCP was orders of magnitude below saturation. Nor is strip current relevant towards predicting the nonlinearity

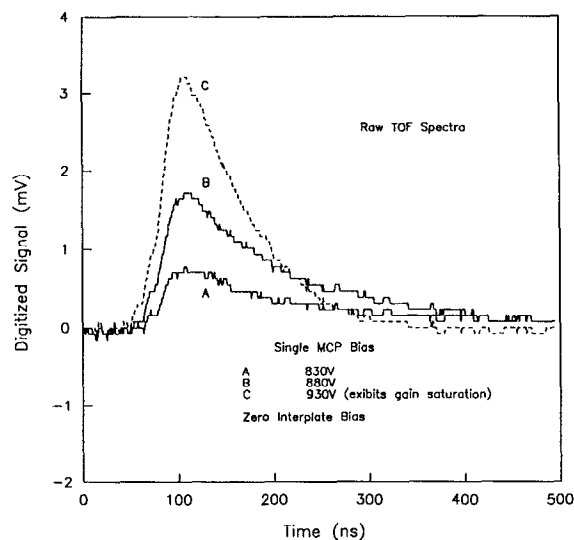


FIG. 7. 256 shot average TOF spectra from 100 fs laser excitation of Ag(111) showing differing levels of gain saturation between signal leading edge and tail introduced by chevron intraplate bias variation at zero interplate (gap) voltage.

exhibited in C, since during the observation period of 500 ns the average channel resupply was about the same in all three cases ($1000 \text{ V/plate} \div 3 \times 10^8 \Omega$) $\times 500 \text{ ns}$ divided by 2.49×10^6 channels/plate $\sim 4 e^-$ /channel.

By way of introducing methods to either detect or correct for gain saturation in TOF spectra (besides always re-taking the data at several lower plate biases) it is appropriate to briefly review the qualitative understanding of rear MCP gain that emerges from available literature. It has been reported that the typical single channel charge output from the rear MCP of a chevron is much higher than the total per channel gain measured when there is full plate pulsed input saturation of a single MCP.¹⁹ This evidence has given rise to the hypothesis that when many adjacent pores simultaneously fire in the rear MCP, as is typical in chevron operation, each pore can exhaust not only charge stored in the last $\approx 20\%$ of the channel, where most of the gain multiplication occurs, but also, through parallel capacitance, charge stored in adjacent quiescent channels.¹⁹ The anticipated consequence relevant to single pulse profiling apparently is that each incident electron activating a front MCP channel expends all gain available for a time constant τ , in a circular region of the rear MCP constituted by pores that are either directly excited to avalanche or neighboring ones from which charge is cannibalized. We have observed that variations in TOF spectra exemplified by Fig. 7 curves A, B, and C can be reconciled by assuming gain deactivation of quiescent channels neighboring an active pore. In the following phenomenological discussion, the physical identity of the deactivation mechanism will not be presumed. Later on we will readdress the question of the deactivation mechanism.

Representative curves A, B, and C of Fig. 7 can be fit rather well by a formula that assumes progressive gain deactivation in the rear MCP of the generic type discussed above,

$$f_o(t) = f_i(t) G_f(V) G'_r(V) \times \left[\left(N_c - \frac{\int_0^t f_o(t') A_{MCP} dt'}{q(V)} \right) / N_c \right]. \quad (10)$$

Here $f_i(t)$, $f_o(t)$ denote, respectively, front MCP input and rear MCP output electron flux, A_{MCP} is the exposed active area per plate, and $q(V)$ is the ratio of output charge to number of rear MCP channels deactivated by a mechanism to be identified later. Accommodation of an attenuation factor between rear MCP output current and digitizer voltage value and rearrangement of the previous expression yields a more useful though less self explanatory expression,

$$f_i(t_j) = \frac{N(t_j)H}{G_F(V)G'_R(V)A_{MCP}} \times \left[\left(N_c - \frac{\sum_{k=0}^j HN(t_k)\Delta t}{q(V)} \right) / N_c \right]^{-1}, \quad (11)$$

where $N(t_j)$ denotes the digitized trace in millivolts at a particular time, $H = (10^{-3} \text{ V/mV})/[50 \text{ } \Omega (1.602 \times 10^{-19} \text{ C/e}^-)]$ (post-chevron attenuation), and Δt is the time separation between consecutive digitized voltages. In Fig. 8 we show this fit by displaying $(A_{MCP}/N_c)f_i(t)$ given by this equation with data curves A-C of Fig. 7 substituted for $N(t)$ and $G_F(V)G'_R(V)$, $H/q(V)$ as indicated. Some elaboration is desirable regarding the method employed to select these parameters. For small t , we have $f_i(t) = (H/A_{MCP})N(t)/[G_F(V)G'_R(V)]$ and so the ratios $G_F(930 \text{ V})G'_R(930 \text{ V}) : G_F(880 \text{ V})G'_R(880 \text{ V}) : G_F(830 \text{ V})G'_R(830 \text{ V})$ can be obtained by simple inspection of the initial ratios of the three curves in Fig. 7. The indicated values of lumped parameters, $H/q(930 \text{ V})$, $H/q(880 \text{ V})$, $H/q(830 \text{ V})$ yielded closest agreement—Fig. 8—among the corresponding $f_i(t)$. Because of the essentially linear re-

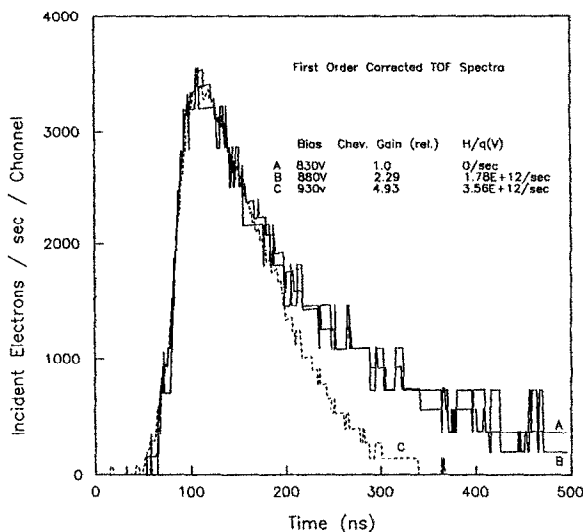


FIG. 8. Reconciliation of TOF spectra recorded at different MCP bias levels (Fig. 7) after corresponding differences in initial chevron gain and gain saturability [$H/q(V)$] are deconvolved to first order.

sponse at 880 and 830 V remarked upon earlier, the search for the best fit was expedited by the approximation of zero gain saturation at 830 V, corresponding to setting $q(830 \text{ V}) = \infty$. It should be noted that qualitatively similar gain deactivation occurs for nonzero chevron interplate voltages (Fig. 9), and the foregoing analysis is applicable to $V_G \neq 0$ data without modification. The digitized TOF spectrum $\{f_i(t_j)\}$ is completely determined, except for a proportionality constant, by the digitized data $\{N(t_j)\}$ and lumped value of $H/q(V)$. The experimental implication of the foregoing analysis is that we have obtained a formula correcting for gain saturation in first order, together with an experimental procedure for obtaining the required correction constants of $H/q(V)$ over a range of chevron operating voltages. This procedure, employed at several chosen operating voltages, calibrates the detector for future data collection as long as the gain characteristics of the MCPs do not deteriorate appreciably. Also, the sought after criterion for detecting gain saturation in the rear MCP is now evident. The rear MCP provides identical gain to all electrons in the incident pulse with measured time of flight t satisfying

$$\frac{H}{q(V)} \int_0^t N(t') dt' \ll N_c. \quad (12)$$

VI. PHYSICAL MODEL OF PORE BLEACHING

In the representative case just described, we were able to correct our data for distortion from progressive rear MCP channel deactivation and attendant gain loss. Assuming that (in first approximation) the instantaneous ratio of rear plate output to deactivated channels remains constant, we obtained best fit values for this ratio, denoted $q(V)$, given that H can be determined. Denoting by N the number of rear MCP channels contained in spot size D , activated by one pore of the front MCP and by N_Q the neighboring quiescent deactivated channels, our measured $H/q(V)$ values can be written as

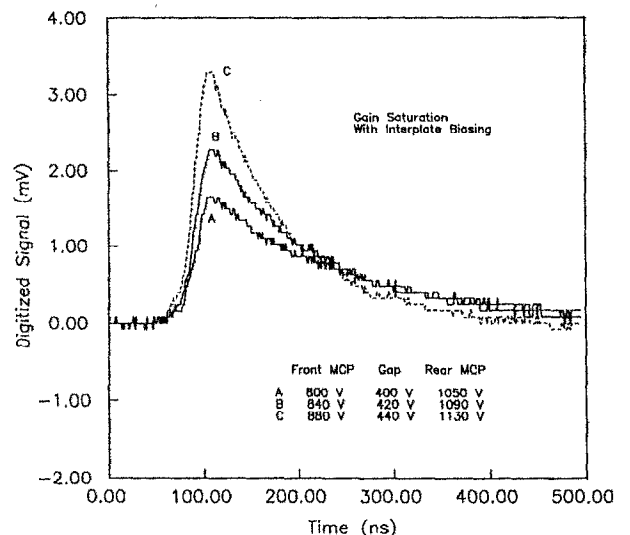


FIG. 9. TOF spectra from Fig. 7 system showing similar gain saturation effects with nonzero interplate bias.

$$\frac{H}{q(V)} = \frac{1.248 \times 10^{14} e^-/s}{[\text{post-chevron attenuation}] G_F(V) G'_R(V) e^-},$$

or

$$N_Q(V) = \left(\frac{H}{q(V)} \right) \frac{G_F(V) G'_R(V)}{1.248 \times 10^{14} s^{-1}} \times [\text{post-chevron attenuation factor}] - N. \quad (13)$$

We may substitute for N using the $V_G = 0$ limit of a formula given by Fraser *et al.*¹⁸ for channel plate spot size,

$$D_s = D + \frac{4V_1^{1/2} d \cos(90^\circ - \Delta\theta)}{2V_1^{1/2} \sin(90^\circ - \Delta\theta)}, \quad (14)$$

and the known pore diameter and open area ratio characterizing our rear MCP. V_1 is the crossover potential, 20 V, to which an electron must be accelerated in order to cause the channel secondary emission coefficient to exceed unity, d is the interplate spacing, D is the pore diameter, and $\Delta\theta = 15^\circ$, a compromise value in the range of 10° – 20° suggested in Ref. 18. According to Audier *et al.*^{18,20} the gain in the rear MCP is given by

$$G'_R(V) = G_R(V) [N/G_F(V)]^\alpha \quad (15)$$

for V in the saturation region of the $G_R(V)$ vs V curve (as is true for all our measurements), where prime denotes chevron as opposed to single plate mode and $\alpha = 0.6$ for a 40:1 MCP. Using these formulae and our chevron characteristics given in Tables I and II, one obtains

$$N = 65, G_F(930 \text{ V}) G'_R(930 \text{ V}) = 5.18 \times 10^6,$$

and

$$G_F(880 \text{ V}) G'_R(880 \text{ V}) = 2.68 \times 10^6.$$

By referencing the experimental data (digitized voltage) corresponding to several known electron fluxes incident on the detector with the manufacturer's gain values for both MCPs and the chevron gain formula of Audier, we were able to estimate the post-chevron attenuation of our system, 0.009. (In later trials we have obtained an attenuation value of 0.3 with no deterioration in response function quality by relocating the dc voltage decoupling gap to the 1-in.-diam flared portion of the signal line (displayed in Fig. 1), but otherwise preserving the same coaxial conductor geometry and biasing. This modification improves signal transmission by increasing the gap coupling capacitance (proportional to gap area) and simultaneously decreasing the parasitic capacitance between anode and ground.) Substituting previously determined values $H/q(930 \text{ V}) = 3.57 \times 10^{12} s^{-1}$, $H/q(880 \text{ V}) = 1.78 \times 10^{12} s^{-1}$, one obtains $N_Q(930$

TABLE II. Varian MCP test data.

Bias(V)	Front MCP gain	Rear MCP gain
800	2.0(3)	3.0(3)
880	4.64(3) ^a	7.48(3) ^a
900	5.3(3)	8.6(3)
930	7.87(3) ^a	11.7(3) ^a
1000	1.3(4)	1.8(4)

^a Author's interpolation.

$V) = 1319$ and $N_Q(880 \text{ V}) = 340$. Since the open area ratio of the plates was 0.65, corresponding radii of deactivated channels in the rear MCP per excited front MCP channel are $23.1 D$ and $12.5 D$ at 930 and 880 V bias, respectively. These deactivation radii are in reasonable agreement with an estimate (in CGS),

$$r_d(t, V) = \frac{\epsilon_r + 1}{\epsilon_r} \left(\frac{G_F(V) G'_R(V) e^-}{I_s} \right) \frac{D e^{-t/\tau}}{V_{or}}, \quad (16)$$

where t denotes the elapsed time since channel excitation, V_{or} the average radial energy per secondary electron, and I_s the channel saturation length. Successive input electrons to the same channel do not change its saturation region wall charge density; since the i th electron gain $G_i = \delta_i \delta^{S/a}$, where S_i is the associated saturation onset location and the average gain, $G_R(N/G_F)^\alpha$ corresponds in first approximation to $i = 0.5 [G_F/N]$, then I_s is given by

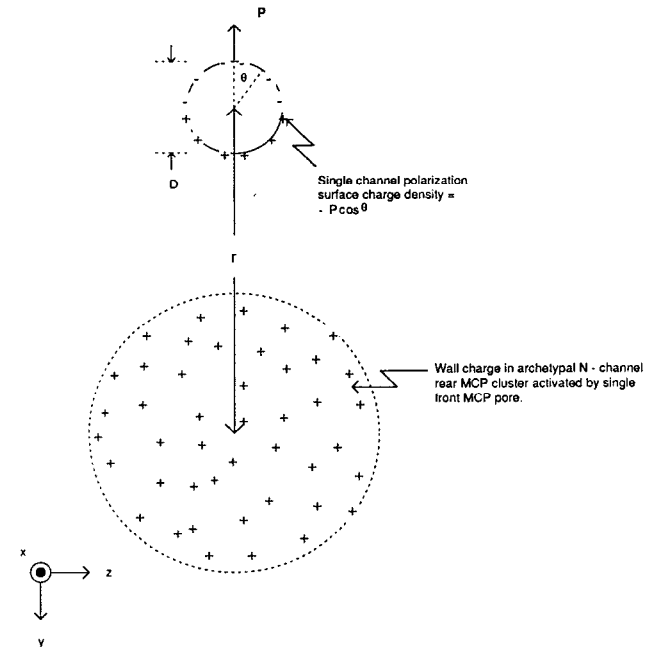


FIG. 10. Estimation of electric field causing gain deactivation in quiescent channels surrounding activated rear MCP cluster. Excluding the single channel shown, remainder of MCP modeled by continuous dielectric with $\mathbf{P} = [(\epsilon_r - 1)/4\pi] \cdot \mathbf{E}$, where

$$\tilde{\epsilon} = \begin{pmatrix} \epsilon_x & 0 & 0 \\ 0 & \epsilon_r & 0 \\ 0 & 0 & \epsilon_r \end{pmatrix}.$$

Electric field strength at the center of single channel is approximately given by $E_{center} = E_{cl}(r) + 2\pi P$, $r \gg D/2$, where $E_{cl}(r) = (2N - \text{channel wall charge})/(\epsilon_r r)$.

TABLE I. Front and rear MCP characteristics.

Type	Varian VUW-8960
R	$3 \times 10^8 \Omega$
L/D	40
OAR	65%
Bias	5°
Active diameter	0.77 in.
D	$10 \mu\text{m}$
N_i	2.06×10^6 (for 0.70 in. aperture)

$$I_s = 2 \left\{ L_{MCP} - \frac{a}{\ln \delta} \ln \left[\frac{G_R}{\delta_1} \left(\frac{N}{G_F} \right)^\alpha \right] \right\},$$

where

$$\delta_1 = [OAR] [(V_1 + V_z)/V_1]^{1/2}, \quad V_z = \frac{V^2 D^{2.13.15}}{L_{MCP}^2 4V_{or}},$$

$$\text{and } \frac{\ln \delta}{a} = \frac{1}{L_{MCP}} \ln \left(\frac{G_R}{\delta_1} \right). \quad (17)$$

Using values of $G_{F,R}$ (V) from Table II, $e^- = 4.8 \times 10^{-10}$ statcoulomb, $\epsilon_r = 8.3$,¹⁴ and $V_{or} = 1.6 \text{ V} \times 1/300$ stat-

volt/V (Ref. 13) this expression yields $r_d(0,930 \text{ V}) = 19.0D$ and $r_d(0,880 \text{ V}) = 10.6D$. The derivation of $r_d(t, V)$ requires initially identifying the mechanism deactivating gain in the quiescent channels surrounding those actually emitting electrons. One possibility has already been raised earlier in discussing the concept of gain deactivation: the suggestion by Eberhardt¹⁹ that charge transfer occurs from neighboring unfired channels to activated ones during chevron discharge. As will be shown later, the low conductivity of the standard MCP matrix, which is well known to prohibit strip current resupply of MCP channels during firing^{13,17} mitigates strongly against this type of recharge also.

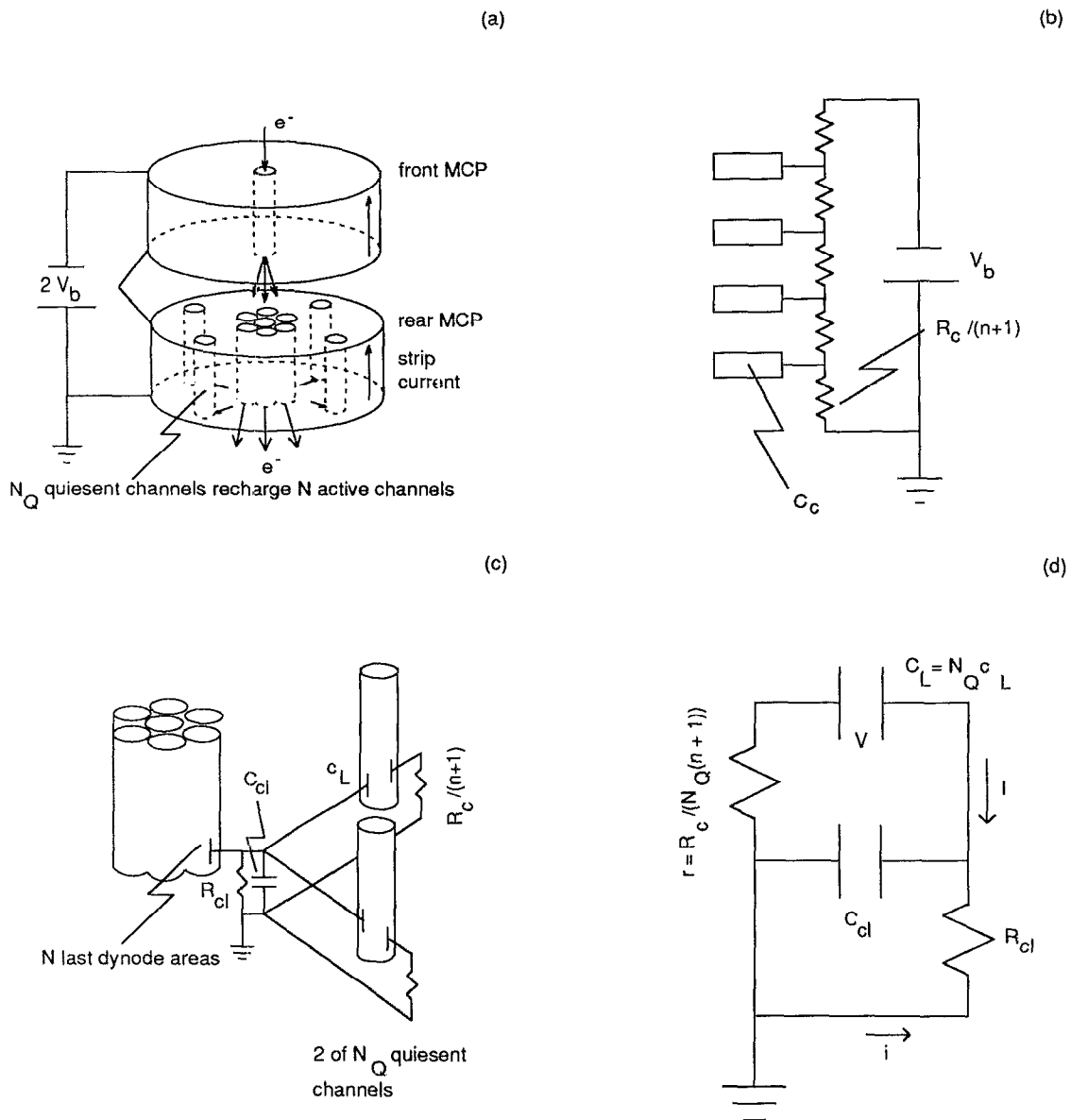


FIG. 11. Analysis of rear MCP active channel recharge rate by neighboring quiescent channels. (a) Schematic of chevron processes. (b) n dynode single channel model. Assuming N_c channels per plate, the channel resistance value $R_c = R_{MCP} N_c$. The last dynode capacitance to ground $C_c = (n+1)C_{MCP}/N_c$. (c) Lumped element model of active cluster recharge (strip current neglected). Since the N last dynodes are equipotential, they can be treated as if connected in parallel with equivalent resistance and capacitance to ground $R_{cl} = R_c/[N(n+1)]$, $C_{cl} = NC_c$. Recharge of the preceding $n-1$ dynode areas (nonprincipal gain source) is neglected. (d) Equivalent circuit of (c). Solution of the circuit equations reveals that active cluster recovery by charge transfer from quiescent channels is slow compared to charge replenishment by strip current.

By a process of elimination, then, one is led to explore the possibility that the field in the proximity of an activated rear MCP cluster interferes significantly with the subsequent gain process in neighboring pores. As is anticipated by the results of Gatti and co-workers (finding strong field leakage from a single active pore into second neighbor channels¹⁶) this is clearly possible, as wall charge equal to $G_F(V)G'_R(V)e^-$ decaying exponentially with time constant

$$R_{\text{MCP}} C_{\text{MCP}} \frac{\text{OAR}}{(1 - \text{OAR})\pi}$$

produces a radial field outside the cluster (and a purely longitudinal field inside the cluster neglecting edge effects) given approximately by

$$E_{\text{cl}}(r) = \frac{2}{\epsilon_r r} \frac{[N - \text{channel wall charge}]}{[\text{charge saturated length}]}. \quad (18)$$

This result is obtained using Gauss' law and neglecting channel end effects including the 5° channel bias. The field, $E_{\text{cl}}(r)$, leads to volume and surface polarization charges as indicated in Fig. 10. At a distance $r \gg D/2$, the single channel radius, the field at the center of an unfired channel is $E_{\text{cl}}(r)$ plus a contribution from the channel polarization surface charge.²¹ The field produced by this polarization surface charge can be approximated to first order by $2\pi P$, using the formula for the field of an infinite line charge. Hence, for $D/2 \ll r < l_s$ [$l_s(930 \text{ V}) = 25.5D$, $l_s(880 \text{ V}) = 23.7D$ in this study], and dropping the nonessential center proviso, we find an approximate perturbing field,

$$E(r) = \frac{\epsilon_r + 1}{\epsilon_r} \frac{1}{r} \left(\frac{G_F(V)G'_R(V)e^-}{l_s} \right). \quad (19)$$

For sufficiently small r this field can cause all wall collisions to occur with so little intervening acceleration via the bias field that secondary emission levels necessary for gain are not achievable: ($\delta \sim \sqrt{KE}/\sqrt{eV_1}$).¹⁵ At a larger radius, where $e^- E(r)D = V_{\text{or}}e^-$, the average radial kinetic energy of secondaries from the channel wall, those with initial transverse velocity parallel to $E(r)$ will generally impact far down the channel, if at all, and consequently experience relatively small gain. One can therefore estimate that strong gain disturbance extends at least through the region $E(r)D \gg V_{\text{or}}$, giving immediately the earlier mentioned deactivation radius.

In order to establish the foregoing analysis of chevron gain saturation, it is necessary to consider the extent to which current from quiescent channels replenishes wall charge in an active cluster of rear MCP channels. This possibility was suggested in earlier work modeling MCPs with discrete dynodes.¹⁹ The essential idea in its most viable form is summarized in Fig. 11. A determination of the rate at which the last dynodes of the N active channels are recharged by the combined available lateral capacitance C_L reduces to solving the indicated equivalent circuit in Fig. 11(d). The Kirchoff equations relevant to this circuit

$$V + (Q_{\text{cl}}/C_{\text{cl}}) - Ir = 0, \quad (20)$$

$$V + iR_{\text{cl}} - Ir = 0, \quad (21)$$

$$\dot{Q}_{\text{cl}} = -I - i, \quad (22)$$

$$(Q_{\text{cl}}/C_{\text{cl}}) - iR_{\text{cl}} = 0, \quad (23)$$

together with $V = -Q_L/C_L$ and $I = \dot{Q}_L$ yield

$$\dot{Q}_{\text{cl}} + \frac{R_{\text{cl}}C_{\text{cl}} + C_L(R_{\text{cl}} + r)}{rR_{\text{cl}}C_{\text{cl}}C_L} Q_{\text{cl}} + \frac{Q_{\text{cl}}}{rR_{\text{cl}}C_{\text{cl}}C_L} = 0. \quad (24)$$

One finds cluster recharge by neighboring quiescent channels proceeds as $Q_{\text{cl}}(t) = Q_{\text{cl}}(0) \exp(-t/\tau_{\text{rchg}})$ where $\tau_{\text{rchg}} \approx R_{\text{cl}}C_L$ under the expectation¹⁹ that $C_L \gg C_{\text{cl}}$. Since (Fig. 11) $R_{\text{cl}}C_{\text{cl}} = R_{\text{MCP}}C_{\text{MCP}}$, $C_L \gg C_{\text{cl}}$ implies the relation $\tau_{\text{rchg}} \gg R_{\text{MCP}}C_{\text{MCP}}$. For our 1 in. diam, 0.017-in.-thick plates, $R_{\text{MCP}} = 3 \times 10^8 \Omega$, $C_{\text{MCP}} = 30$ pf, yielding $\tau_{\text{rchg}} \gg 9$ ms; since our experimentally observed gain deactivation occurs during a data acquisition period of only 500 ns, lateral capacitive charge removal from quiescent channels is too slow to cause the observed gain deactivation. It is also likely that were charge depletion in quiescent channels mainly responsible for their deactivation, $q(V) \equiv$ (rear MCP e^- output/deactivated channel) would be expected to increase with V rather than decrease as shown in Fig. 8.

ACKNOWLEDGMENTS

The authors are pleased to acknowledge assistance from Martin Kitka for providing drawings used to develop the tapered anode assembly, and assistance from M. C. Downer and W. Banyai during femtosecond excitation tests of the detector. This work was sponsored by JSEP F49620-89-C-0044 and by the National Science Foundation DMR89-22359.

¹ R. W. Schoenlein, W. Z. Lin, J. G. Fujimoto, and G. L. Eesley, Phys. Rev. Lett. **58**, 1680 (1987).

² S. I. Anisimov, B. L. Kapeliovich, and T. L. Perelman, Sov. Phys. JETP **39**, 375 (1975).

³ J. G. Fujimoto, J. M. Liu, E. P. Ippen, and N. Bloembergen, Phys. Rev. Lett. **53**, 1837 (1984).

⁴ K. Giesen, F. Hage, F. J. Himpel, H. J. Riess, and W. Steinmann, Phys. Rev. Lett. **55**, 300 (1985).

⁵ R. W. Schoenlein, J. G. Fujimoto, G. L. Eesley, and T. W. Capehart, Phys. Rev. Lett. **61**, 2596 (1988).

⁶ J. Bokor, Science **246**, 1130 (1989).

⁷ M. C. Downer, W. C. Banyai, M. W. Wood, D. C. Anacker, and J. L. Erskine, Proc. SPIE **1209**, 166 (1990).

⁸ W. C. Banyai, D. C. Anacker, X. Y. Wang, D. H. Reitze, G. B. Focht, M. C. Downer, and J. L. Erskine, J. Opt. Soc. Am. (in press).

⁹ W. C. Banyai, D. C. Anacker, X. Y. Wang, D. H. Reitze, G. B. Focht, M. C. Downer, and J. L. Erskine, International Conference on Quantum Electronics Technical Digest Series 1990 (Optical Society of America, Washington, DC, 1990), Vol. 8, p. 268.

¹⁰ J. Bokor, R. Haight, R. H. Storz, J. Stark, R. R. Freeman, and P. H. Bucksbaum, Phys. Rev. B **32**, 3669 (1985).

¹¹ E. W. Plummer, Nucl. Instrum. Methods **177**, 179 (1980).

¹² D. W. O. Hedde, J. Phys. E **4**, 589 (1971).

¹³ C. Loty, Acta Electron. **14**, 107 (1971).

¹⁴ J. L. Wiza, Nucl. Instrum. Methods **169**, 587 (1979).

¹⁵ E. H. Eberhardt, Appl. Opt. **18**, 1418 (1979).

¹⁶ E. Gatti, K. Oba, and P. Rehak, IEEE Trans. Nucl. Sci. **NS-30**, 461 (1983).

¹⁷ G. W. Fraser, Nucl. Instrum. Methods **221**, 115 (1984).

¹⁸ G. W. Fraser, J. F. Pearson, G. C. Smith, M. Lewis, and M. A. Barstow, IEEE Trans. Nucl. Sci. **NS-30**, 455 (1983).

¹⁹ E. H. Eberhardt, IEEE Trans. Nucl. Sci. **NS-28**, 712 (1981).

²⁰ M. Audier, J. C. Delmotte, and J. P. Boutot, Rev. Phys. Appl. **13**, 188 (1978).

²¹ J. E. Jackson, Classical Electrodynamics, 2nd ed. (Wiley, New York, 1975), p. 136.